Journal of Materials Chemistry

Cite this: J. Mater. Chem., 2012, 22, 21767

www.rsc.org/materials

PAPER

Enhancing the current density of electrodeposited ZnO–Cu_2O solar cells by engineering their heterointerfaces†

Ahmad Sabirin Zoolfakar,*[ad] Rozina Abdul Rani,[a] Anthony J. Morfa,[b] Sivacarendran Balendhran,[a] Anthony P. O'Mullane,[c] Serge Zhuiykov[e] and Kourosh Kalantar-zadeh*[a]

Received 10th May 2012, Accepted 3rd September 2012
DOI: 10.1039/c2jm35682a

Using ZnO seed layers, an efficient approach for enhancing the heterointerface quality of electrodeposited ZnO–Cu_2O solar cells is devised. We introduce a sputtered ZnO seed layer followed by the sequential electrodeposition of ZnO and Cu_2O films. The seed layer is employed to control the growth and crystallinity and to augment the surface area of the electrodeposited ZnO films, thereby tuning the quality of the ZnO–Cu_2O heterointerface. Additionally, the seed layer also assists in forming high quality ZnO films, with no pin-holes, in a high pH electrolyte solution. X-ray electron diffraction patterns, scanning electron and atomic force microscopy images, as well as photovoltaic measurements, clearly demonstrate that the incorporation of certain seed layers results in the alteration of the heterointerface quality, a change in the heterojunction area and the crystallinity of the films near the junction, which influence the current density of photovoltaic devices.

1. Introduction

The development of low cost, efficient and reliable solar cells is an important goal for managing the growing global energy demand and reducing greenhouse gas emissions.[1] Metal oxide semiconductors are ideal for thin film based solar cells, as many of them are thermally and photo-stable, earth-abundant, have tuneable electronic properties, can be structurally controlled, and offer excellent characteristics for forming a wide range of heterojunction based devices.[2,3]

Thin film photovoltaic devices made of n-type zinc oxide (ZnO) and p-type cuprous oxide (Cu_2O) heterojunctions have attracted increasing interest due to their theoretical power conversion efficiency (PCE) of 18% and an absorption coefficient higher than single crystalline Si.[4,5] ZnO thin films have favourable characteristics for developing solar cells including their transparency, wide band gap (3.37 eV) and high electron mobility ($\sim$120 $cm^2\ V^{-1}\ s^{-1}$).[6,7] Cu_2O is also a well-known oxide semiconductor for solar cell applications. Cu_2O is a direct band gap material with a band gap of 2.1 eV.[8] It has a high absorption coefficient in the visible region and the minority carrier diffusion length is also suitable for use as a solar cell absorber layer.[9] Overall, both materials are inexpensive, abundant, and non-toxic which are obvious benefits for solar cell technologies.[8,10,11] Despite such advantages, in practice the ZnO–Cu_2O solar systems have never reached high efficiencies.[7,12,13] This is due to the fact that theoretically their intrinsic electronic band structure does not allow any open-circuit voltage values larger than 0.7 V.[13] For as-electrodeposited ZnO–Cu_2O bilayer cells, open-circuit voltages no higher than 0.32 V have been reported.[7,9,12] By doping the ZnO layer in such heterojunctions, it is possible to increase the efficiency by reducing the internal resistance.[12] Doping also reduces the effect of interface states as a result of a better distribution of charges at the heterointerface. In these cases, an open circuit voltage as large as 0.69 V has been reported.[14]

Though ZnO doping is essential for increasing the efficiency of ZnO–Cu_2O solar cells, it is still imperative to investigate how the crystallinity and heterointerface morphologies can affect such devices. Any improvement in the efficiency, photocurrent or voltage of the as-deposited ZnO–Cu_2O offers an excellent pathway, ultimately, for the doped ZnO–Cu_2O systems. The maximum current density ever reported for an undoped electrodeposited bilayer of ZnO–Cu_2O under AM 1.5 illumination has been 8.2 mA cm^{-2} by Cui and Gibson.[15] In the report, the ZnO film had a nanowire morphology and they suggested that this high current density was due to the large surface area of the heterojunction.[15] This report, together with many others, suggests that increasing the surface to volume ratio, together with high crystallinity of the ZnO and Cu_2O layers, is the most

[a]*School of Electrical and Computer Engineering, RMIT University, Melbourne, VIC 3001, Australia. E-mail: a.zoolfakar@student.rmit.edu.au; kourosh.kalantar@rmit.edu.au*
[b]*School of Chemistry & Bio21 Institute, University of Melbourne, ParkVille, Victoria, 3010, Australia*
[c]*School of Applied Sciences, RMIT University, Melbourne VIC 3001, Australia*
[d]*Faculty of Electrical Engineering, Universiti Teknologi MARA, 40450 Shah Alam, Malaysia*
[e]*Materials Science and Engineering Division, CSIRO, Highett, VIC, Australia*

† Electronic supplementary information (ESI) available. See DOI: 10.1039/c2jm35682a

important way to obtain large current densities for the ZnO–Cu_2O heterojunction devices.[7,12,13,15]

ZnO and Cu_2O can be prepared using different methods such as thermal oxidation,[16] electrodeposition,[4,15,17–19] anodic oxidation,[20] pulsed laser deposition,[21] spraying,[22] thermal evaporation,[23,24] nanoparticle inks,[25] dc reactive magnetron sputtering[26] and rf reactive magnetron sputtering deposition.[27–29] Among the aforementioned methods, electrodeposition has several advantages such as low fabrication costs, facile control over film thickness, morphology and doping concentration, low temperature and low ambient pressure processing.[4,30] In addition, post-annealing processes can be avoided as the deposited films are highly crystalline.[4] All these factors are important for developing cost-effective and efficient photovoltaic technologies. As a result, ZnO–Cu_2O heterojunction solar cells based on electrodeposition methods have attracted significant attention.[7,9,15,18,31] However, obtaining rough surfaces that increase the surface to volume ratio, hence increasing the heterointerface and solar cell current density, has been a challenge. Many conventional electrodeposition methods of ZnO produce highly crystalline films which is the parameter that is highly sought after in heterojunction solar cells but often have low surface roughness.[7,15] The electrodeposited ZnO crystallites generally follow the topography of the substrates and well-engineered tuning methods are required to modify their morphologies into nanocrystallites with low dimensions.[32–34] There are recent reports by Cui and Gibson[15] and Musselman *et al.*[13] describing the use of growth directing agents such as hexamethylenetetramine (HMT) and potassium chloride (KCl) to reduce the radius of the electrodeposited nanowires. However in their ZnO films, the spacing between the nanowires was still more than ideal and many of the nanowires were criss-crossed as they were not all grown normal to the heterojunction surface. There are also concerns regarding this method as the formation of pin-holes and inhomogeneity of the films can occur due to the solubility of ZnO in high pH electrolytes, which are generally used for the electrodeposition of Cu_2O.[7,9,35] During the electrodeposition process, pin-holes can be filled by Cu_2O, forming ohmic contacts with the conductive glass-substrate, which is detrimental, as it degrades the performance of the solar cells.

We, amongst many other groups, have previously shown that the application of a ZnO seed layer can significantly enhance the surface to volume ratio of hydrothermally deposited ZnO films.[29,36–40] Peterson *et al.* were among the first to exploit the advantages of radio frequency (rf) sputtered ZnO seed layers. They have reported that a seeding layer on substrates can significantly affect the nucleation and growth of ZnO nanowires in a hydrothermal process.[38] They believed that the interfacial tension between solution species and crystal nucleation sites depend on the degree of structural fits, the same crystal type having the best fit and lowest energy barrier.[38] In this work, we introduce seed layers of ZnO deposited by a rf sputtering technique before the electrodeposition process due to two fundamental motivations: (a) to tune the morphology of the electrodeposited ZnO grains to increase the surface to volume ratio of the heterojunction and (b) to tune ZnO and Cu_2O nucleation in order to obtain a highly crystalline phase of ZnO and Cu_2O, for films with excellent homogeneity and no pin-holes. The ZnO seed layers are formed under different deposition conditions to alter their crystallinity, adhesion properties of the interfaces and grain morphologies. By introducing the ZnO seed layer approach, we show their effect on the electrodeposited ZnO films and their surface roughnesses, and on ZnO–Cu_2O heterojunctions as well as their photovoltaic performance.

2. Experimental

2.1 Materials

Zinc nitrate ($Zn(NO_3)_2$) (Aldrich, 98%), copper(II) sulphate ($CuSO_4$, Aldrich, 99%), lactic acid ($C_3H_6O_6$, Aldrich, 85%), and sodium hydroxide (NaOH, Aldrich, 99%) were used in the experiments. All solvents were of analytical grade and solutions were prepared using Milli-Q water with a resistivity of 18.2 MΩ cm. All chemicals and solvents were used without further purification.

2.2 Growth and characterisation of ZnO

Commercially available fluorine doped tin oxide (FTO) coated glass-substrates with a sheet resistance of 15 Ω per square were purchased from Dyesol. The substrates were cut into rectangles of 10 mm × 25 mm, sonicated in acetone, and rinsed in isopropanol and deionized water to remove any organic contaminations. Seed layers of ZnO were directly deposited on the substrates using the rf sputtering techniques, which are described below. Then, thin layers of ZnO films were electrodeposited onto the samples.

In the sputtering process, the target was ZnO of 4 inches diameter and 99.99% purity. The sputtering chamber was pumped to an ultimate background pressure of 10^{-5} Torr and the sputtering pressure increased to 20×10^{-3} Torr. Our goal in this approach was to find the deposition parameters for obtaining an optimum seed layer to enhance the ZnO nucleation, crystal morphology and quality, as well as heterointerface adhesion properties. As a result, during the deposition, the sputtering rf power was set at different values ranging from 60 to 110 W. The argon and oxygen gas concentration ratio in the chamber was kept constant at 60% and 40%, respectively. The substrates' deposition duration and temperature were fixed at 60 minutes and 260 °C, respectively. The target to substrate distance was set at 65 mm.

Electrodeposited ZnO films were prepared from an acidic aqueous solution containing 0.05 M zinc nitrate. The seed layers were used as the working electrode, in a 3 electrode setup consisting of a Ag/AgCl reference electrode and a zinc sheet (99.99% purity) as a counter electrode. The deposition temperature was fixed at 62 °C by using a water bath heater as suggested by Izaki and Omi.[41] Cyclic voltammetry (CV) measurements were conducted first to determine the deposition potentials of the thin films. The CV measurements were carried out using a CHI410A electrochemistry workstation (CH Instruments). Then, the ZnO thin films were electrodeposited at a constant potential of −0.7 V without stirring. The deposition time was varied from 300 to 2000 s for finding the optimum thickness for the solar cells.

2.3 Growth and characterisation of electrodeposited Cu_2O on ZnO

Cu_2O films were electrodeposited on ZnO/FTO/glass substrates using an alkaline aqueous solution containing 0.4 M copper(II) sulphate and 3 M lactic acid as a chelating agent. The solution pH was adjusted to 13.5 by adding sodium hydroxide. The electrodeposition process was carried out potentiostatically at −0.55 V and the deposition time was varied from 1000 to 2500 s. During the electrodeposition process, the solution was kept at 40 °C without stirring, as suggested by Izaki *et al.*[18] To avoid the etching of ZnO films in the Cu_2O growth solution, the negative potential is applied immediately after immersing the samples in the solution to avoid any possible surface corrosion. A high purity graphite rod was used as a counter electrode and Ag/AgCl was used as the reference electrode.

2.4 Materials and device characterisation

The crystallographic properties of the films were studied using an X-ray diffraction (XRD – Bruker D8 DISCOVER) micro-diffractometer fitted with a GADDS (General Area Detector Diffraction System) using CuKα radiation ($\lambda = 1.54178$ Å) and Raman spectroscopy (Renishaw 1000 micro-Raman system). In addition, scanning electron microscopy (SEM – FEI Nova NanoSEM) and atomic force microscopy (AFM – Bruker MultiMode 8 with PF TUNA) were utilized to analyze the morphology and structural properties of the films. Circular Au contact pads with a diameter of 5.6 mm were sputtered on top of the ZnO–Cu_2O structures. Photovoltaic measurements were recorded employing an ABET technologies solar simulator with an AM 1.5 spectrum distribution. Electrical and photovoltaic property effects were studied using a Keithley 2602 source meter. The incident photon-to-electron conversion efficiency (IPCE) measurements were carried out using a customized Newport IPCE setup with no light biasing. Measurements were conducted at short-circuit with reference to a calibrated Si photodiode (Peccell Limited, S1337-1010BQ).

3. Results and discussions

Fig. 1(a,c–f) shows the SEM top view images of films resulting from variable sputtering power set to 60, 80, 100 and 110 W, respectively. The thickness of the films ranged from 200 to 300 nm upon increasing the power. The ZnO films were composed of columnar grains in a direction normal to the substrate surface, with the base of the grains changing depending on the sputtering power. The ZnO grains were found to be densely packed in all cases. In addition, all films seem to have coral-like structures composed of irregular facades that enhance the surface roughness of the films.

As can be seen from Fig. 1(a,c) at a low sputtering power of 60 W, the main grains were made of much smaller sub-grains. Interestingly at 80 W, the dimensions of the main grains became dominant and the sub-grains completely disappeared (Fig. 1(a,d)). The size of the main grains increased when the power was elevated to 100 W and eventually to 110 W (Fig. 1(a,e) and 1(a,f), respectively). The increase in grain size can be due to the fact that at higher powers, ions obtain more energy prior to collision with the substrate.[42] Such high-energy ions are capable of adjusting their bond direction and length in order to obtain optimum bonding to the adjacent atoms, promoting vigorous nucleation that contributes to the grains dimensions.[42]

The electrodeposition of ZnO films was conducted as described in the "Experimental" section. The mechanism for the electrodeposition of ZnO films is outlined in eqn (1)–(3). Initially nitrate ions are reduced at the ZnO seed electrode, which raises the electrolyte pH at the solid–solution interface *via* the production of hydroxide ions as shown in eqn (1). In the presence of zinc ions in the electrolyte $Zn(OH)_4^{2-}$ is formed (eqn (2)), which converts to ZnO in a dehydration process (eqn (3)), which occurs rapidly at temperatures higher than 50 °C.[43,44]

$$NO_3^- + H_2O + 2e^- \rightarrow NO_2^- + 2OH^- \quad (1)$$

$$Zn^{2+} + 2OH^- + 2H_2O \rightarrow Zn(OH)_4^{2-} + 2H^+ \quad (2)$$

$$Zn(OH)_4^{2-} + 2H^+ \rightarrow ZnO + 3H_2O \quad (3)$$

There are two factors that need to be controlled during the ZnO electrodeposition process: temperature and applied potential.[41,44] In order to minimise the formation of metallic Zn in the films and promote the process outlined in eqn (1)–(3), the electrodeposition process needs to be carried out at temperatures equal to or greater than 50 °C.[44] In addition, the applied potential must not be too negative so as to avoid hydrogen evolution at the working electrode which would be detrimental to the quality of the electrodeposited film. Therefore, CV experiments were carried out at 62 °C to elucidate the most appropriate electrodeposition potential for the fabrication of ZnO. Fig. 2 shows CVs for the electrodeposition of ZnO on five different samples: samples with different seed layers and also blank FTO for comparison. From the current–voltage traces, it is apparent that there is a significant overpotential required for the electrodeposition of ZnO on FTO compared to the seed ZnO layers. Fig. 3 shows the SEM image of ZnO films electrodeposited onto FTO, demonstrating poor coverage and isolated clusters of ZnO. This shows that the ZnO seed layer is required to increase the adhesion of the ZnO nuclei to the substrate surface. The rougher surface of the seed layer promotes formation of adatoms, which group to form a stable ZnO nucleus.[45]

Fig. 1(b,c–f) show the SEM images of ZnO films that were electrodeposited on different rf sputtered seed layers. For the film deposited on the 60 W seed layer, the ZnO nanostructures were composed of irregularly shaped grains as shown in Fig. 1(b,c). The inter-grain spacing was significantly larger than all other samples and many of the grains were loosely placed on the surface. Formation of these loose and isolated ZnO crystals can be observed clearly throughout the films. It is suspected that nucleation is inhibited within the space between the large seed grains and the growth rate of ZnO may be reduced within these areas due to the diffusion-limited availability of the source materials.[15] For the 80 W seed layer, the electrodeposited grains show uniformly distinctive hexagonal morphologies with clear boundaries (Fig. 1(b,d)). For the 100 W seed layer, the hexagonal grain size continued to increase but became less dense compared to the 80 W seed layer case as shown in Fig. 1(b,e). For the 110 W seed layer, the ZnO grains continued to increase in size. However, they significantly deviate from their hexagonal shape

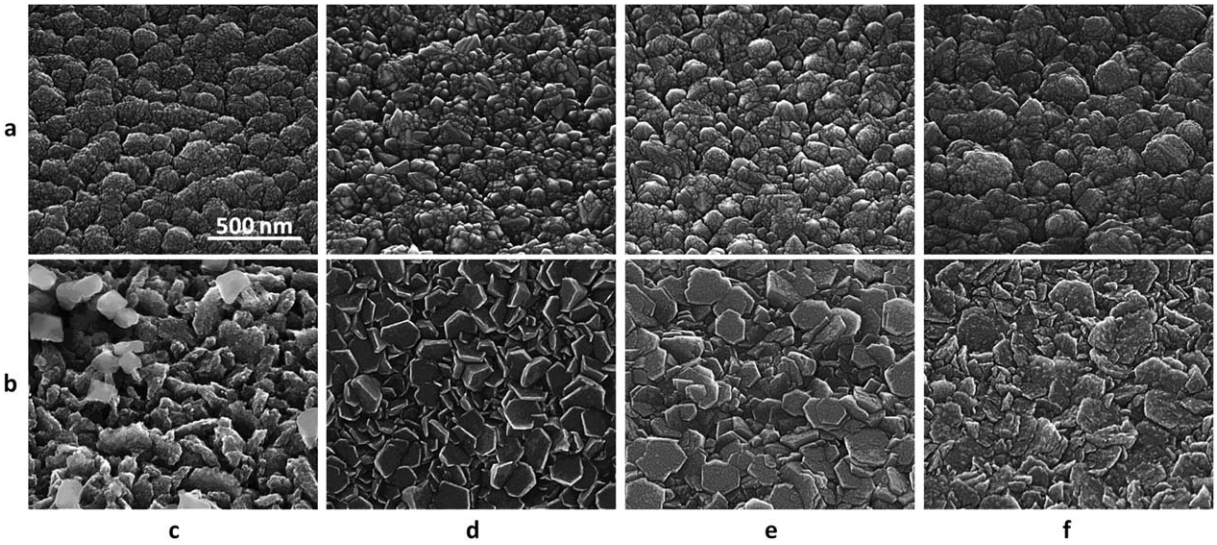

Fig. 1 SEM images of the surface of ZnO samples (a,c–f) rf sputtered, (b,c–f) electrodeposited under various sputtered powers, (c) 60 W, (d) 80 W, (e) 100 W and (f) 110 W. Scale bars are similar for all figures.

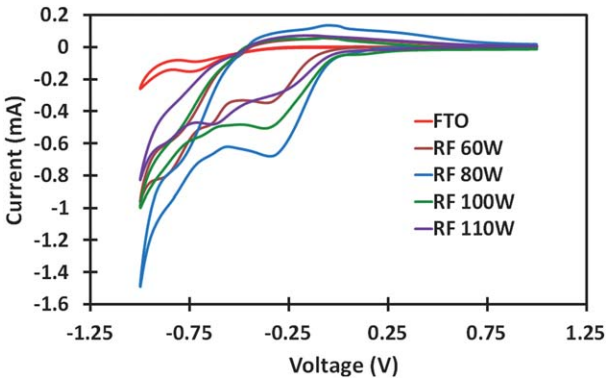

Fig. 2 Cyclic voltammetry of electrodeposited ZnO layers on different rf sputtered ZnO films on FTO glass substrates as well as a blank FTO for comparison.

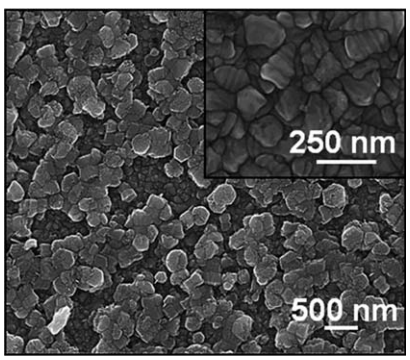

Fig. 3 Top view SEM image of an electrodeposited ZnO on the FTO glass substrate without a seed layer. Inset: SEM image of the FTO surface.

and flake like structures with irregular shapes (Fig. 1(b,f)) appeared. For the films electrodeposited onto 80, 100 and 110 W seed layers, the resultant films consisted of densely packed grains with no evidence of pores. The SEM images clearly show that the morphology of the ZnO seed layers significantly influenced the packing density and shape of the grains in the electrodeposited ZnO films and allowed the crystallinity and morphology of the material to be controlled.

From the CV data, the electrodeposited film formed onto the 80 W seed layer has the highest reduction peak magnitude at −0.31 V. This cathodic process is due to the reduction of nitrate at the working electrode as stated in eqn (1). A further rise in cathodic current beyond −0.75 V is most likely due to the direct reduction of Zn^{2+} ions to Zn metal as reported previously.[44,46] At potentials more negative than −0.90 V a sharp increase in current was detected due to the hydrogen evolution reaction. On the reverse sweep a small anodic peak was observed at −0.50 V, which is due to stripping of Zn metal from the electrode. Here it is clear that the onset potential for ZnO growth is −0.025 V and therefore a potential of −0.70 V was chosen to ensure ZnO growth while avoiding both Zn metal electrodeposition and hydrogen evolution. Interestingly, the magnitude of the reduction peak decreases significantly for the other seed layers of 60, 100, and 110 W respectively, as well as a slight shift to a more negative potential indicating a more inhibited reduction process. This is probably due to the surface morphology and grain sizes of the seed layers. Smaller grain sizes and increased surface roughness increase both the ease and rate of reduction of the nitrate ions and hence ZnO formation. This suggests defect site driven growth, in particular when compared to the FTO case, which is a much smoother electrode material. Significantly, this results in more densely packed films.

The effect of the seed layers on the surface morphology of the electrodeposited ZnO films were studied using AFM. It has been reported that the morphologies and crystal size of ZnO seed layers affect the quality of the hydrothermally deposited ZnO.[47] Breedon *et al.* reported that the growth of ZnO nanostructured arrays from HMT assisted solutions on rf sputter coated ZnO substrates is a function of the sputtered crystallite sizes.[36] Wang *et al.* pointed out that films deposited on ZnO seeds of the (002) preferred orientation led to well-defined hexagonal facet (002)

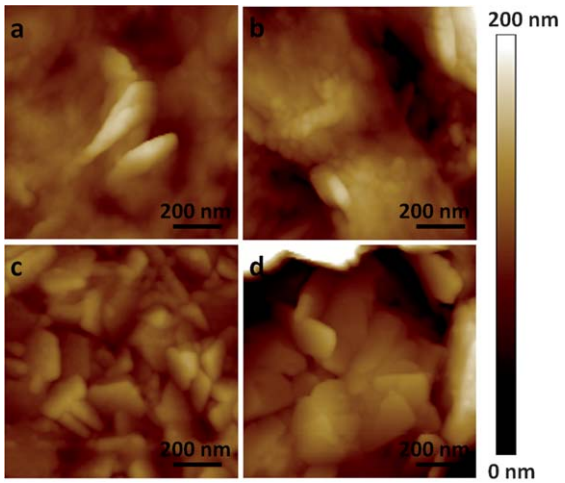

Fig. 4 AFM images of electrodeposited ZnO thin films grown onto different rf sputtered ZnO seed layers (a) 60 W, (b) 80 W, (c) 100 W and (d) 110 W.

ZnO nanorods grown nearly vertical to the substrates.[48] Our work used the same concept but for electrodeposited ZnO films.

Fig. 4 shows the two-dimensional (2D) AFM images of the electrodeposited ZnO films formed onto different seed layers using various sputtering powers. The 60 W seed layer resulted in (Fig. 4(a)) the smallest surface roughness of the electrodeposited layer with the root mean square (RMS) value of ~12 nm. As the sputtering power increased to 80 W, the surface roughness of the electrodeposited layer increased, showing an RMS value of ~34 nm (Fig. 4(b)). Further, increasing the sputtering power to 100 and 110 W decreased the surface roughness of the electrodeposited layer to ~28 (Fig. 4(c)) and ~25 nm (Fig. 4(d)), respectively. Larger surface roughnesses are expected to increase the heterointerface area between the p–n junctions.[49] Therefore, for films with similar crystallinity, we expect that the electrodeposited film onto the 80 W seed layer would produce the largest current density. Crystallinity of the films is investigated next.

The phases of the obtained ZnO samples were investigated using XRD measurements. Fig. 5(a) shows the XRD patterns of the seed layers resulting from variable sputtering powers. The films deposited were crystalline in nature with a wurtzite structure which appear in the crystal orientation of (100), (002), (101), (102), (110), (103) and (112) matching ICDD no. [21-1486]. The XRD patterns also show clearly resolved diffraction peaks originating from the FTO substrate noted with asterisks, ICDD no. [41-1445]. At the lower sputtering power of 60 W, the ZnO crystal orientations of (100), (002), (101), (102), (110) and (103) were weak and could barely be resolved. This confirms the SEM observation that the ZnO films were made of smaller sub-grains, which did not receive enough energy to form larger dimensions. Additionally, the films are also the thinnest at this low sputtering power due to smaller growth rates. After increasing the sputtering power to 80 W, the peak intensity, especially for the preferred orientation (002) peak, showed a significant increase compared to the other crystal orientations. By further increasing the power to 100 W, all the wurtzite peaks could be clearly observed, especially the crystal orientation of (103).

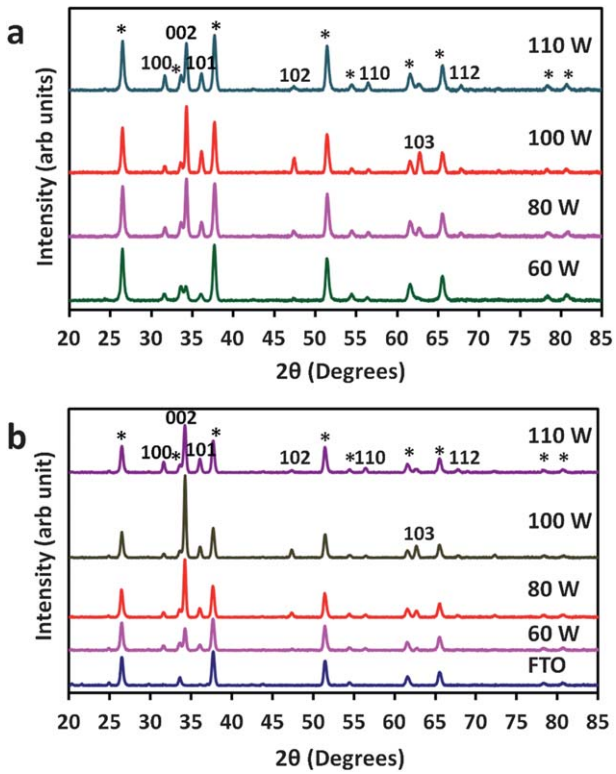

Fig. 5 XRD patterns of ZnO films (a) rf sputtered at different applied powers and (b) electrodeposited. FTO is indicated with an *.

Interestingly, the preferred orientation (002) peak intensity decreased with the increase of power to 110 W. At high powers, ZnO films became non-stoichiometric due to oxygen deficiency which led to the growth of less homogeneous films with more crystallographic faults[50] as also observed in our SEM images (Fig. 1(a,f)).

Fig. 5(b) shows the XRD patterns for the electrodeposited ZnO layers on different ZnO seed layers and a blank FTO for comparison. For the ZnO film electrodeposited on a blank FTO, the intensity of the ZnO crystal peaks was almost immeasurable and FTO diffraction peaks dominated the pattern. This is due to the poor coverage of ZnO films on the substrate as seen in Fig. 3. For the electrodeposited film onto the 60 W seed layer, all ZnO crystal orientations of (100), (002), (101), (102), (110), (103) and (112) peaks can be observed. Most of the peaks were weak as the SEM image also revealed that the grains were randomly oriented on the surface. For the higher power seed layer of 80 W, the crystallinity of the electrodeposited ZnO film improved significantly, especially evidenced by the increase in the intensity of the (002) peak. In confirmation, uniformly distinctive hexagonal morphologies with clear boundaries could also be observed in the SEM images (Fig. 1(b,d)). This increase was continued further for the sample with the 100 W seed layer. Interestingly, the (002) ZnO peak emerged as the dominant peak, indicating the presence of ordered ZnO to a large extent. For the 110 W seed layer, peaks corresponding to the (100) and (101) planes show an increase in their intensities, indicating better crystallinity towards (100) and (101) planes in comparison with the film obtained at lower sputtering powers (see ESI† for further characterisation).

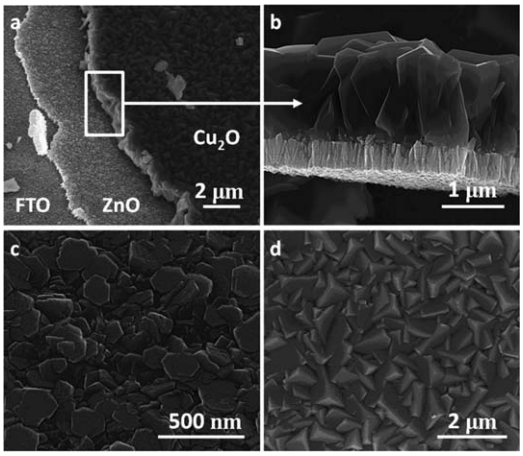

Fig. 6 SEM images of surface morphology and cross-section (a) top view image of ZnO–Cu_2O on a FTO glass substrate, (b) 45° tilted image of the ZnO–Cu_2O heterojunction, (c) top view image of an electrodeposited ZnO film and (d) top view image of an electrodeposited Cu_2O film.

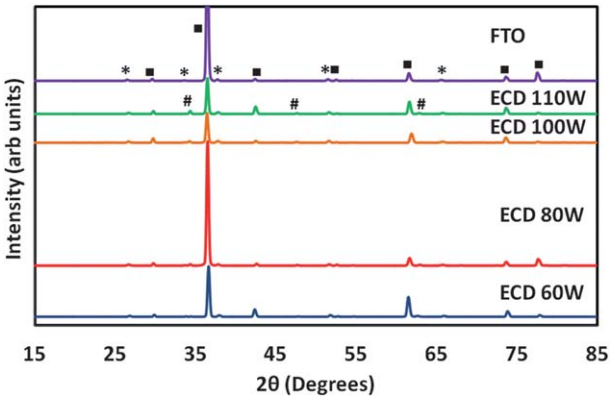

Fig. 7 XRD patterns for ZnO–Cu_2O films: the ZnO electrodeposited films are formed onto rf sputtered ZnO seed layers, which are deposited onto FTO. For comparison, the XRD pattern of the electrodeposited Cu_2O onto electrodeposited ZnO without any seed layer is also demonstrated. FTO is indicated with an *, ZnO is indicated with a #, and Cu_2O is indicated with a ■.

Fig. 6 shows SEM micrographs of the ZnO–Cu_2O heterojunction by electrodepositing Cu_2O (of 1.8 μm thickness) on top of the ZnO films (only the sample incorporating the electrodeposited ZnO onto the 80 W seed layer is demonstrated). Cu_2O was formed according to the following electrochemical reaction:[18]

$$2Cu^{2+} + 2e^- + 2OH^- \rightarrow Cu_2O + H_2O \quad (4)$$

The electrodeposition process was carried out potentiostatically at −0.55 V and the deposition time was varied from 1000 to 2500 s. During the electrodeposition process, the solution was kept at 40 °C without stirring as suggested by Izaki *et al.*[18] The Cu_2O film was composed of columnar grains grown in the direction normal to the substrate surface. No defects, such as pores or pin-holes, were observed on the surface or throughout the film thickness. Top and cross-sectional views shown in Fig. 6(a) and (b) indicate that the ZnO and Cu_2O films clearly establish a rough heterointerface between the films. Fig. 6(c) and (d) show the crystal grains of ZnO and Cu_2O, respectively.

The composition of the electrodeposited ZnO–Cu_2O heterojunction was analyzed using the XRD measurements. Fig. 7 shows the XRD patterns of films comprising Cu_2O on ZnO electrodeposited onto ZnO seed layers, resulting from sputtering powers of 60, 80, 100, and 110 W and blank FTO. The XRD pattern of ZnO–Cu_2O without a seed layer reflects the dominant peak at a 2θ value of 36.5° corresponding to the (111) plane of Cu_2O (ICDD no. [75-1531]). Secondary peaks at 29.6°, 42.4°, 52.6°, 61.5°, 73.7° and 77.6° corresponding to (110), (200), (211), (220), (311) and (222) planes of Cu_2O, respectively, were also observed. Peaks corresponding to ZnO were barely resolved. However, devices with seed layers show ZnO peaks at 34.4°, 47.5° and 62.9° corresponding to the (002), (102) and (103) planes of ZnO, respectively. At a low sputtering power of 60 W, strong Cu_2O peaks of (111), (200) and (220) dominated the films. At a higher sputtering power of 80 W and 100 W, the films were dominated by the (111) planes of Cu_2O, indicating the presence of ordered Cu_2O to a larger extent.[15,51] However, at the larger power of 110 W, the (111) Cu_2O crystal plane was no longer dominant as other crystal orientations such as (200) and (220) peaks appeared with intensities significantly larger than achieved when Cu_2O was electrodeposited onto films that had seed layers fabricated at the lower power of 80 and 100 W films. This indicates that Cu_2O in this film is highly crystalline with a random distribution of cuprous oxide crystals. In all measurements, weak ZnO peak intensities were observed due to the presence of ZnO underneath the Cu_2O films (see ESI† for Raman spectra characterisation).

In order to further understand the effects of ZnO seed layers at the heterointerface of the electrodeposited ZnO–Cu_2O, AFM adhesion mapping was carried out on the electrodeposited ZnO thin films grown onto different rf sputtered ZnO seed layers (Fig. 8). The adhesion mapping is determined by the contact region difference between tip-approach and tip-retract while scanning the surface of the films (Fig. S3, see ESI† for details). A strong adhesion is clear when a high difference in the horizontal (z) position of the jump-to-contact and jump-to-off-contact points occurs. The amount of force just before the jump-off-contact gives a measurement of the maximum tip–sample adhesion. The corresponding sample adhesion, which is measured by this force, is then translated into an image as a function of the (x,y) position. The dark areas of the adhesion mapping images correspond to lower adhesion to the surface, relative to other areas of the surface. The films formed using a 60 W seed layer surface (Fig. 8(a)) show the greatest adhesion compared to the rest of the samples. Interestingly, as the sputtering power increased to 80 W (Fig. 8(b)) and 100 W (Fig. 8(c)), the surface adhesion properties of the electrodeposited layer decreased significantly. By further increasing the sputtering power to 110 W, the adhesion of the films increased but was lower than the 60 W sample (Fig. 8(d)).

It seems that the higher adhesive nature of the surface significantly reduces the heterointerface quality (which is in agreement with the SEM images of the interfaces in Fig. S4, ESI†). It is found that a highly adhesive surface hinders the formation of highly crystalline Cu_2O, which is also confirmed by the XRD patterns as shown in Fig. 7.

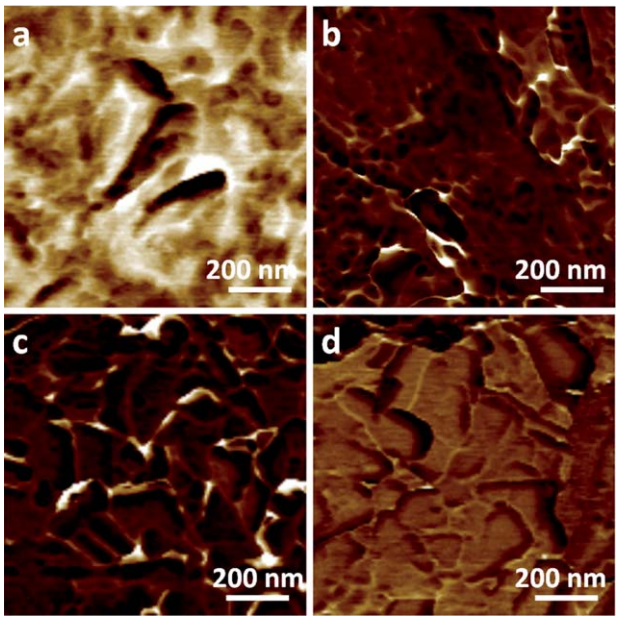

Fig. 8 AFM adhesion images (arbitrary units) of electrodeposited ZnO thin films grown onto different rf sputtered ZnO seed layers (a) 60 W, (b) 80 W, (c) 100 W and (d) 110 W. The dark areas correspond to lower adhesion.

In order to probe the effect of rf sputtered seed layers on interface morphology and material composition and the subsequent effect on electrical conduction, photovoltaic devices were prepared. The photovoltaic power conversion efficiencies (PCEs) of electrodeposited ZnO–Cu_2O devices were studied by measuring the current density–voltage (J–V) characteristics at simulated AM 1.5 solar illumination (100 mW cm^{-2}). Illumination was through the FTO substrate.

The schematic of the developed ZnO–Cu_2O heterojunction solar cells is illustrated in Fig. 9(a). The photovoltaic J–V curves for different ZnO–Cu_2O heterojunctions under AM 1.5 illumination are shown in Fig. 9(b) and the corresponding parameters of the measured solar cells are summarized in Table 1. We fixed the optimum electrodeposition duration for ZnO and Cu_2O at 1000 s and 2000 s, respectively (see ESI†). The thicknesses of the electrodeposited ZnO films were found to be consistent even though different seed layers were used. It can be concluded that the ZnO seed layers have less significant influence on the final thickness of the ZnO film compared to morphology or crystallinity of the films.

The ZnO–Cu_2O film heterojunction prepared on a blank FTO (*i.e.* without using any seed layer of ZnO) exhibited the lowest PCE of 0.09% with an open circuit voltage (V_{oc}) of 0.071 V, a short circuit current density (J_{sc}) of 5.25 mA cm^{-2} and a fill factor (FF) of 23.87%. As mentioned previously, on the blank FTO, the ZnO electrodeposition process only produced a poor coverage as shown in Fig. 3. The effect was even more exacerbated due to the solubility of ZnO in the high pH solution for the deposition of Cu_2O, leading to the formation of pinholes throughout the ZnO layer. These pinholes were then filled by Cu_2O and formed shunted diodes and a short circuit between the FTO glass substrate and the electron conductor layer.

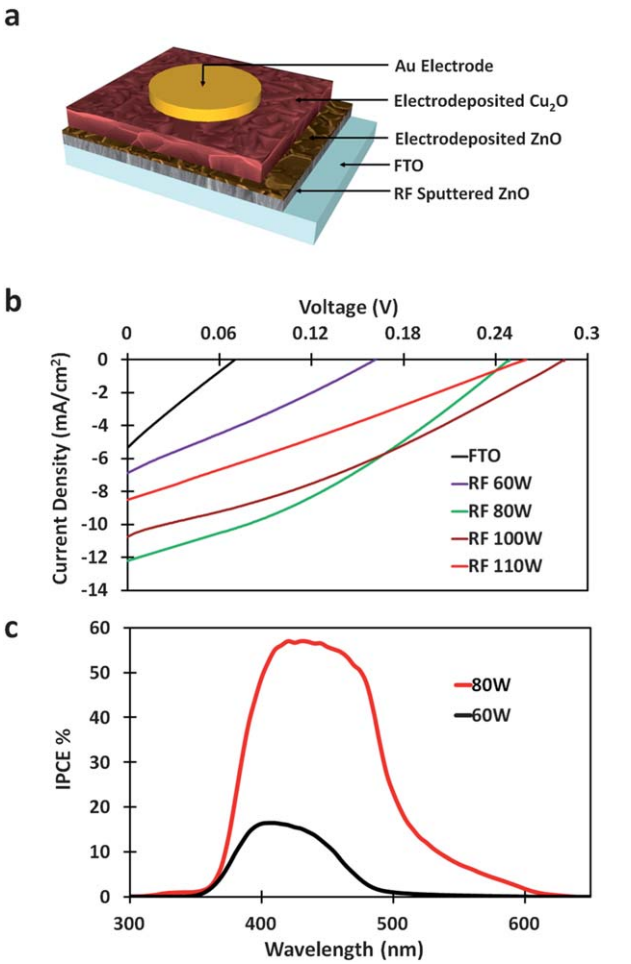

Fig. 9 Schematic and characteristic curves of the ZnO–Cu_2O based heterojunction solar cells. (a) The 3D schematic of the electrodeposited ZnO–Cu_2O solar cells incorporating different rf sputtered ZnO seed layers, and (b) J–V characteristic curves of four types of ZnO–Cu_2O heterojunction solar cells. For comparison the response of the electrodeposited ZnO–Cu_2O without any seed layer is also demonstrated. (c) The IPCE spectra of ZnO–Cu_2O based heterojunction solar cells incorporating 60 and 80 W sputtered seed layers.

Table 1 Photovoltaic properties of five types of ZnO–Cu_2O solar cells obtained from Fig. 9

Solar cell	J_{sc} (mA cm^{-2})	V_{oc} (V)	FF (%)	PCE (%)
FTO	5.25	0.071	23.87	0.09
RF 110 W	8.51	0.262	26.10	0.58
RF 100 W	10.84	0.285	31.35	0.95
RF 80 W	12.78	0.248	32.40	1.02
RF 60 W	6.83	0.161	27.19	0.30

The solar cells performance improved significantly when thin layers incorporating ZnO seed layers were used. The combination of rf sputtered seed layer and electrodeposited ZnO layers promoted the formation of stable ZnO nuclei, resulting in more robust ZnO films. Therefore, pin-hole problems were successfully resolved.

The ZnO–Cu_2O heterojunction device prepared with a seed layer of 60 W produced the lowest photovoltaic properties

among the other seed layers with V_{oc}, J_{sc}, FF and PCE of 0.161 V, 6.83 mA cm^{-2}, 27.19%, and 0.30%, respectively. This is most likely due to the poor crystallinity of the ZnO and Cu_2O films (due to the small intensity of (111) for Cu_2O – a result of higher ZnO surface adhesive properties, Fig. 8(a) – and (002) for ZnO films) as well as the lower heterointerface surface roughness, as demonstrated by the AFM measurements (Fig. 4(a)). In addition, the formation of isolated ZnO crystallites as shown in Fig. 1(b,c) possibly increased the internal resistance of the films and reduced the current density of the device.

As we increased the rf power of the seed layer to 80 W, the photovoltaic properties of the device significantly enhanced. V_{oc}, J_{sc}, FF and PCE increased to 0.248 V, 12.7 mA cm^{-2}, 32.40% and 1.02%, much larger than the device incorporating the 60 W seed layer. As demonstrated using AFM, XRD and SEM characterizations, this can be due to a combination of the increase in the junction interface area, higher surface roughness, lower adhesion at the heterointerface and better crystallinity of both ZnO and Cu_2O films. Fig. 1(b,d) clearly show that the ZnO grains have uniformly distinctive and perfect hexagonal morphologies.

However, further increasing the sputtering power of the incorporated seed layer to 100 W did not improve the photovoltaic properties any further. Although the hexagonal grain dimensions continued to increase, less densely packed grains were observed compared to the 80 W case as shown in Fig. 1(b,e). This resulted in a decrease in surface roughness as confirmed by the AFM measurements. This factor may explain the reduction of short circuit current density from 12.7 to 10.8 mA cm^{-2} for devices incorporating 80 and 100 W seed layers, respectively. Interestingly, the open circuit voltage increased slightly from 0.248 to 0.285 V. This can be ascribed to a decrease in the interface states density at the heterointerface due to the reduction of the surface to volume ratio. This limits the unwanted band bending and carrier recombination of the film. A full explanation about the interface states is discussed thoroughly by Musselman *et al.*[12] To summarize, if a significant number of states exist at the interface of the heterojunction films that act as acceptors, electrons may be removed from the depletion region and bend the energy band of Cu_2O upwards. Upward band bending in Cu_2O near the interface would therefore reduce the open circuit voltage of the device.[12] Interface state density has direct correlation with the surface to volume ratio between p–n junctions. A larger surface to volume ratio produces more interface states.[12]

As expected, increasing the sputtering power to 110 W further deteriorated the solar cell performance. J_{sc}, V_{oc} and PCE showed a small decrease in comparison with 100 W but still much higher than 60 W. As the rf power increased to 110 W, the ZnO grains continued to increase in size and lost their hexagonal shape and eventually converted to flake like structures with irregular morphologies (Fig. 1(b,f)). As a result, J_{sc} was reduced to 8.51 mA cm^{-2}. Obviously, the decrease of J_{sc} reduces the PCE. The same trend is expected for further increasing the sputtering power. In order to verify the reproducibility of the solar cells performance, we fabricated six different samples for each type of ZnO–Cu_2O heterojunction solar cells and obtained the average values (see ESI†).

The IPCE spectra of solar cells obtained using 60 and 80 W ZnO seed layers are shown in Fig. 9(c). These two solar cells were chosen as they presented the highest and lowest PCEs. As expected, the peak magnitude of the IPCE spectrum of the device which incorporated the 80 W seed layer was four times larger than its 60 W counterpart, showing a maximum conversion efficiency of 57.2% in comparison to 15.8%. These numbers indicate that the larger surface area between the p–n junction and the improved crystallinity of the electrodeposited ZnO films has a positive effect on the IPCE. From the measured IPCE and known solar spectrum, J_{sc} can be predicted ($J_{sc} = q\int \mathrm{AM}\ 1.5(\lambda) \times \mathrm{IPCE}(\lambda) \times \mathrm{d}\lambda$). The measured J_{sc} under AM 1.5 illumination is higher than the calculated J_{sc} for both of the J–V curves that can be ascribed to the charge trapping affect in the low light intensity IPCE measurements.[9,52,53]

Our work suggests that the improvement of photovoltaic properties can be achieved by tuning the growth conditions, adhesion properties of the heterointerfaces, crystal quality and morphology of ZnO film prior to Cu_2O growth. Although the best PCE value (1.02%) in this research is still less than the highest value previously reported in the literature for electrodeposited films,[18] obvious improvements were achieved by the introduction of the ZnO seed layer into the ZnO–Cu_2O heterojunction solar cells. Our current density is the largest ever reported for such a heterojunction (12.7 mA cm^{-2}). Enhanced ZnO nucleation sites, improved Cu_2O crystal quality, as well as large heterojunction areas and increased resistance to high pH solutions, which avoid pinholes, are amongst the positive factors resulting from the introduction of ZnO seed layers.

4. Conclusions

This work demonstrates the effect of ZnO seed layers on the electrodeposited ZnO films in ZnO–Cu_2O heterojunctions as well as their photovoltaic performance of such devices. By incorporating rf sputtered ZnO seed layers, we were able to tune the growth conditions, adhesion properties of the ZnO layer surface, crystal quality, morphology and surface roughness of the interfaces between the electrodeposited ZnO and Cu_2O films in order to produce excellent heterojunctions with greater surface to volume ratios. The seed layer also proved to be effective in ensuring pinhole-free films. These factors enabled our as-deposited ZnO–Cu_2O heterojunction solar cells to reach a relatively high photovoltaic performance of 1.02% for seed layers which were deposited at 80 W. In addition to this, the current density obtained was the largest ever reported (12.7 mA cm^{-2}) for such a heterojunction.

Notes and references

1 V. Fthenakis, J. E. Mason and K. Zweibel, *Energy Policy*, 2009, **37**, 387–399.
2 K. L. Chopra, P. D. Paulson and V. Dutta, *Prog. Photovoltaics*, 2004, **12**, 69–92.
3 J. Jasieniak, B. I. MacDonald, S. E. Watkins and P. Mulvaney, *Nano Lett.*, 2011, **11**, 2856–2864.
4 B. M. Fariza, J. Sasano, T. Shinagawa, H. Nakano, S. Watase and M. Izaki, *J. Electrochem. Soc.*, 2011, **158**, 621–625.
5 S. M. Sze and K. K. Ng, *Physics of Semiconductor Devices*, John Wiley and Sons, New Jersey, 2007.
6 C. M. Lieber, *Solid State Commun.*, 1998, **107**, 607–616.
7 H. Wei, H. Gong, Y. Wang, X. Hu, L. Chen, H. Xu, P. Liu and B. Cao, *CrystEngComm*, 2011, **13**, 6065–6070.
8 A. E. Rakhshani, *Solid-State Electron.*, 1986, **29**, 7–17.

9 S. S. Jeong, A. Mittiga, E. Salza, A. Masci and S. Passerini, *Electrochim. Acta*, 2008, **53**, 2226–2231.
10 S. Jeong and E. S. Aydil, *J. Cryst. Growth*, 2009, **311**, 4188–4192.
11 J. Katayama, K. Ito, M. Matsuoka and J. Tamaki, *J. Appl. Electrochem.*, 2004, **34**, 687–692.
12 K. P. Musselman, A. Marin, A. Wisnet, C. Scheu, J. L. MacManus-Driscoll and L. Schmidt-Mende, *Adv. Funct. Mater.*, 2011, **21**, 573–582.
13 K. P. Musselman, A. Wisnet, D. C. Iza, H. C. Hesse, C. Scheu, J. L. MacManus-Driscoll and L. Schmidt-Mende, *Adv. Mater.*, 2010, **22**, E254–E285.
14 T. Minami, Y. Nishi, T. Miyata and J. Nomoto, *Appl. Phys. Express*, 2011, **4**, 62301.
15 J. B. Cui and U. J. Gibson, *J. Phys. Chem. B*, 2010, **114**, 6408–6412.
16 A. Mittiga, E. Salza, F. Sarto, M. Tucci and R. Vasanthi, *Appl. Phys. Lett.*, 2006, **88**, 163502.
17 E. W. Bohannan, L. Y. Huang, F. S. Miller, M. G. Shumsky and J. A. Switzer, *Langmuir*, 1999, **15**, 813–818.
18 M. Izaki, T. Shinagawa, K.-T. Mizuno, Y. Ida, M. Inaba and A. Tasaka, *J. Phys. D: Appl. Phys.*, 2007, **40**, 3326–3329.
19 S. Xu and Z. L. Wang, *Nano Res.*, 2011, **4**, 1013–1098.
20 A. Roos and B. Karlsson, *Sol. Energy Mater.*, 1983, **7**, 467–480.
21 N. Kikuchi and K. Tonooka, *Thin Solid Films*, 2005, **486**, 33–37.
22 D. A. Firmansyah, T. Kim, S. Kim, K. Sullivan, M. R. Zachariah and D. Lee, *Langmuir*, 2009, **25**, 7063–7071.
23 A. H. Jayatissa, K. Guo and A. C. Jayasuriya, *Appl. Surf. Sci.*, 2009, **255**, 9474–9479.
24 L. S. Huang, S. G. Yang, T. Li, B. X. Gu, Y. W. Du, Y. N. Lu and S. Z. Shi, *J. Cryst. Growth*, 2004, **260**, 130–135.
25 A. J. Morfa, G. Beane, B. Mashford, B. Singh, E. Della Gaspera, A. Martucci and P. Mulvaney, *J. Phys. Chem. C*, 2010, **114**, 19815–19821.
26 C. L. Chu, H. C. Lu, C. Y. Lo, C. Y. Lai and Y. H. Wang, *Physica B*, 2009, **404**, 4831–4834.
27 Y. M. Lu, J. Y. Chen and T. S. Wey, *Mater. Res. Soc. Symp. Proc.*, 2004, **822**, 55–64.
28 Y. M. Lu, W. S. Hwang, W. Y. Liu and J. S. Yang, *Mater. Chem. Phys.*, 2001, **72**, 269–272.
29 J. L. Campbell, M. Breedon, K. Latham and K. Kalantar-zadeh, *Langmuir*, 2008, **24**, 5091–5098.
30 B. J. Plowman, S. K. Bhargava and A. P. O'Mullane, *Analyst*, 2011, **136**, 5107–5119.
31 B. M. Fariza, J. Sasano, T. Shinagawa, S. Watase and M. Izaki, *Thin Solid Films*, 2011, 2261–2264.
32 V. Donderis, M. A. Hernández-Fenollosa, L. C. Damonte, B. Marí and J. Cembrero, *Superlattices Microstruct.*, 2007, **42**, 461–467.
33 X. J. Huang, O. Yarimaga, J. H. Kim and Y. K. Choi, *J. Mater. Chem.*, 2009, **19**, 478–483.
34 A. I. Inamdar, S. H. Mujawar, S. B. Sadale, A. C. Sonavane, M. B. Shelar, P. S. Shinde and P. S. Patil, *Sol. Energy Mater. Sol. Cells*, 2007, **91**, 864–870.
35 S. J. Limmer, E. A. Kulp and J. A. Switzer, *Langmuir*, 2006, **22**, 10535–10539.
36 M. Breedon, J. Yu, W. Wlodarski and K. Kalantar-Zadeh, in *International Conference on Nanoscience and Nanotechnology*, 2008, pp. 9–12.
37 S.-J. Park, J. Qiu, W. He, W. Namgung, Y.-D. Kim, J.-H. Lee, Y.-H. Hwang and H.-K. Kim, *J. Nanosci. Nanotechnol.*, 2009, **9**, 6993–6997.
38 R. B. Peterson, C. L. Fields and B. A. Gregg, *Langmuir*, 2004, **20**, 5114–5118.
39 H. Zeng, J. Cui, B. Cao, U. Gibson, Y. Bando and D. Golberg, *Sci. Adv. Mater.*, 2010, **2**, 336–358.
40 H. Zeng, X. Xu, Y. Bando, U. K. Gautam, T. Zhai, X. Fang, B. Liu and D. Golberg, *Adv. Funct. Mater.*, 2009, **19**, 3165–3172.
41 M. Izaki and T. Omi, *Appl. Phys. Lett.*, 1996, **68**, 2439–2440.
42 X. H. Yu, J. Ma, F. Ji, Y. H. Wang, X. J. Zhang, C. F. Cheng and H. L. Ma, *J. Cryst. Growth*, 2005, **274**, 474–479.
43 C. V. Manzano, D. Alegre, O. Caballero-Calero, B. Alen and M. S. Martin-Gonzalez, *J. Appl. Phys.*, 2011, **110**, 043538.
44 A. Chatterjee and J. Foord, *Diamond Relat. Mater.*, 2006, **15**, 664–667.
45 J. Cembrero and D. Busquets-Mataix, *Thin Solid Films*, 2009, **517**, 2859–2864.
46 A. I. Inamdar, S. H. Mujawar, S. R. Barman, P. N. Bhosale and P. S. Patil, *Semicond. Sci. Technol.*, 2008, **23**, 085013.
47 B. Weintraub, Z. Zhou, Y. Li and Y. Deng, *Nanoscale*, 2010, **2**, 1573–1587.
48 S. F. Wang, T. Y. Tseng, Y. R. Wang, C. Y. Wang and H. C. Lu, *Ceram. Int.*, 2009, **35**, 1255–1260.
49 Y.-M. Shen, C.-S. Chen, P.-C. Yang, S.-Y. Ma and C.-F. Lin, *Sol. Energy Mater. Sol. Cells*, 2012, **99**, 263–267.
50 S.-S. Lin, J.-L. Huang and D.-F. Lii, *Surf. Coat. Technol.*, 2004, **176**, 173–181.
51 L. Wu, L.-k. Tsui, N. Swami and G. Zangari, *J. Phys. Chem. C*, 2010, **114**, 11551–11556.
52 P. E. de Jongh and D. Vanmaekelbergh, *J. Phys. Chem. B*, 1997, **101**, 2716–2722.
53 T. Trupke, P. Wurfel and I. Uhlendorf, *J. Phys. Chem. B*, 2000, **104**, 11484–11488.